International Journal of Applied Earth Observations and Geoinformation 102 (2021) 102422

Contents lists available at ScienceDirect

International Journal of Applied Earth Observations and Geoinformation

journal homepage: www.elsevier.com/locate/jag

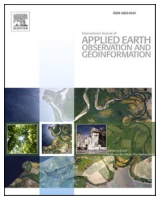

Monitoring, analyzing and predicting urban surface subsidence: A case study of Wuhan City, China

Qing Ding [a], Zhenfeng Shao [a,*], Xiao Huang [b], Orhan Altan [c], Qingwei Zhuang [a], Bin Hu [a]

[a] State Key Laboratory of Information Engineering in Surveying, Mapping and Remote Sensing, Wuhan University, Wuhan 430079, China
[b] Department of Geosciences, University of Arkansas, Fayetteville, AR 72701, USA
[c] Department of Geomatics Engineering, Istanbul Technical University, Istanbul 36626, Turkey

ARTICLE INFO

Keywords:
Urban surface subsidence
Synthetic aperture radar interferometry
Geo-detector
Long short-term memory network

ABSTRACT

Wuhan, one of China's megacities with rapid development, is facing serious surface subsidence. In this study, we combined MT-InSAR, geo-detector, and LSTM (Long Short-Term Memory) to achieve the monitoring, analysis, and prediction of surface subsidence in the main urban districts of Wuhan. The effectiveness of MT-InSAR in monitoring surface subsidence was validated against leveling results. During the monitoring period, the maximum subsidence velocity and uplift velocity were −53.3 mm/year and 18.0 mm/year, respectively. We identified six subsidence regions and explored their deformation characteristics. Further, we analyzed the relationship between the surface subsidence and influencing factors using the geo-detector in a quantitative manner. Our study revealed that the distance to soft soils had the greatest explanatory power on the subsidence. However, we also confirmed that subsidence was affected via coupling effects from multiple factors, suggesting a complex reinforcing relationship among influencing factors. The interaction between the distance to soft soils and the distance to karst collapse prone areas had the largest joint explanatory power on subsidence. Further, we constructed a data-driven LSTM model to predict and analyze the subsidence. The results showed that the LSTM model achieved great performance and presented strong universality, suggesting that it can be used for subsidence prediction in large geographic areas.

1. Introduction

Surface subsidence, one of the most ubiquitous environmental-geological issues, has attracted wide attention (Lorenzo et al., 2020; Lu et al., 2019; Qu et al., 2015). As a continuous and cumulative geological hazard, the developing process of subsidence is considerably slow but difficult to reverse, leading to adverse consequences that include wall cracks, road damages, and even casualties (Amelung et al., 1999; Babaee et al., 2020; Du et al., 2018). In this context, large-scale and high-precision surface subsidence monitoring, analyzing and predicting can provide important supports for the prevention and control of geological disasters.

Despite that D-InSAR (Differential Interferometric Synthetic Aperture Radar) has been widely applied in deformation monitoring caused by surface subsidence (Cigna et al., 2012; Zhou et al., 2015), challenges still remain for D-InSAR in terms of monitoring small long-term deformation due to atmospheric delay and decorrelation. To overcome these limitations, several MT-InSAR (Multi-Temporal InSAR) methods were proposed successively (Berardino et al., 2002; Ferretti et al., 2000; Zhang et al., 2011, 2014). Among them, PS-InSAR (Persistent Scatterer InSAR) is suitable for monitoring targets with high coherence, SBAS-InSAR (Small Baseline Subset InSAR) shortens the spatiotemporal baselines of interferograms so as to obtain more densely distributed monitoring points. Due to its advancement, MT-InSAR has been widely used in monitoring surface subsidence in both urban and rural areas (Li et al., 2013; Osmanoğlu et al., 2011; Perissin et al., 2012; Wang et al., 2019).

Despite the existing MT-InSAR-based efforts to monitor surface subsidence, few studies investigate the potential of predicting subsidence via time-series approaches. The prediction of surface subsidence benefits early warning of geological disasters. Early efforts tend to use numerical and empirical models to predict subsidence (Deng et al., 2017; Kim et al., 2010). However, the applicable potential of these methods is often limited by prior knowledge, and most of them are only

* Corresponding author at: No. 129 Luoyu Road, Hongshan District, Wuhan 430079, Hubei, China.
E-mail addresses: dingqing@whu.edu.cn (Q. Ding), shaozhenfeng@whu.edu.cn (Z. Shao), xh010@uark.edu (X. Huang), oaltan@itu.edu.tr (O. Altan), zhuangqingwei@whu.edu.cn (Q. Zhuang), hubin763259288@whu.edu.cn (B. Hu).

https://doi.org/10.1016/j.jag.2021.102422
Received 6 April 2021; Received in revised form 25 June 2021; Accepted 26 June 2021
Available online 9 July 2021
1569-8432/© 2021 The Authors. Published by Elsevier B.V. This is an open access article under the CC BY-NC-ND license (http://creativecommons.org/licenses/by-nc-nd/4.0/).

applicable to subsidence prediction given specific patterns. In contrast, LSTM (Long Short-Term Memory) network can realize the efficient and accurate prediction of massive time-series data by considering the nonlinearity and time dependence of historical data, which has shown excellent performance in different domains, such as air quality index (Xu et al., 2020), precipitation (Luo et al., 2021), and land cover change (Mu et al., 2019). With the rapid development of MT-InSAR, surface deformation monitoring data featured by dense time-series records has become increasingly available, making it possible to adopt a data-driven LSTM network for subsidence prediction.

Under the joint influence of human activities and natural processes, Wuhan is deeply affected by surface subsidence. Efforts have been made to measure subsidence in Wuhan based on MT-InSAR. Bai et al. (2016) analyzed the relationship between subsidence and urban construction and karst geology using Terra-SAR data from 2009 to 2010. Zhou et al. (2017) used Sentinel-1 data to monitor the spatial distribution of subsidence in Wuhan from 2015 to 2016. Han et al. (2020) investigated the spatiotemporal evolution characteristics of subsidence using multi-source SAR data and discussed the inducement of subsidence. Shi et al. (2021) investigated subsidence rates in Wuhan with Sentinel-1 data that covered 2015–2019 and analyzed the relationship between subsidence and engineering geological regions. Jiang et al. (2021) used nearly 300 COSMO-SkyMed images obtained between 2012 and 2019 to monitor the long-term subsidence, aiming to reveal the spatiotemporal variations of subsidence. The majority of the studies belong to qualitative studies but some (e.g. Jiang et al., 2021) provide quantitative insights. Despite the aforementioned efforts, the interaction of contributing factors with their influencing power on the subsidence remains to be underexplored. To our best knowledge, our study marks a pioneering attempt to conduct both quantitative analysis and time-series prediction of subsidence.

To fill the gaps in the existing studies, we monitored, analyzed, and predicted surface subsidence, taking Wuhan as a study case. MT-InSAR and Sentinel-1A data were used to obtain the time-series surface deformation from January 2018 to August 2020. After verifying the accuracy of MT-InSAR results, we further analyzed the spatiotemporal characteristics of surface deformation. In addition, we applied geodetector to quantitatively analyze the relationship between subsidence and nature- and human-induced factors. Finally, we proposed an LSTM model to predict time-series surface subsidence in selected key regions.

2. Study area

Wuhan, located in the east of the Jianghan Plain, is the capital city of Hubei Province. Wuhan covers a total area of 8494 km^2, and its geographical ranges are 29°58′ N-31°22′ N and 113°41′ E-115°05′ E. In terms of administrative division, Wuhan is composed of thirteen districts. The seven main urban districts are Qingshan (QS), Hongshan (HS), Wuchang (WC), Hanyang (HY), Qiaokou (QK), Jianghan (JH), and Jiang ’an (JA).

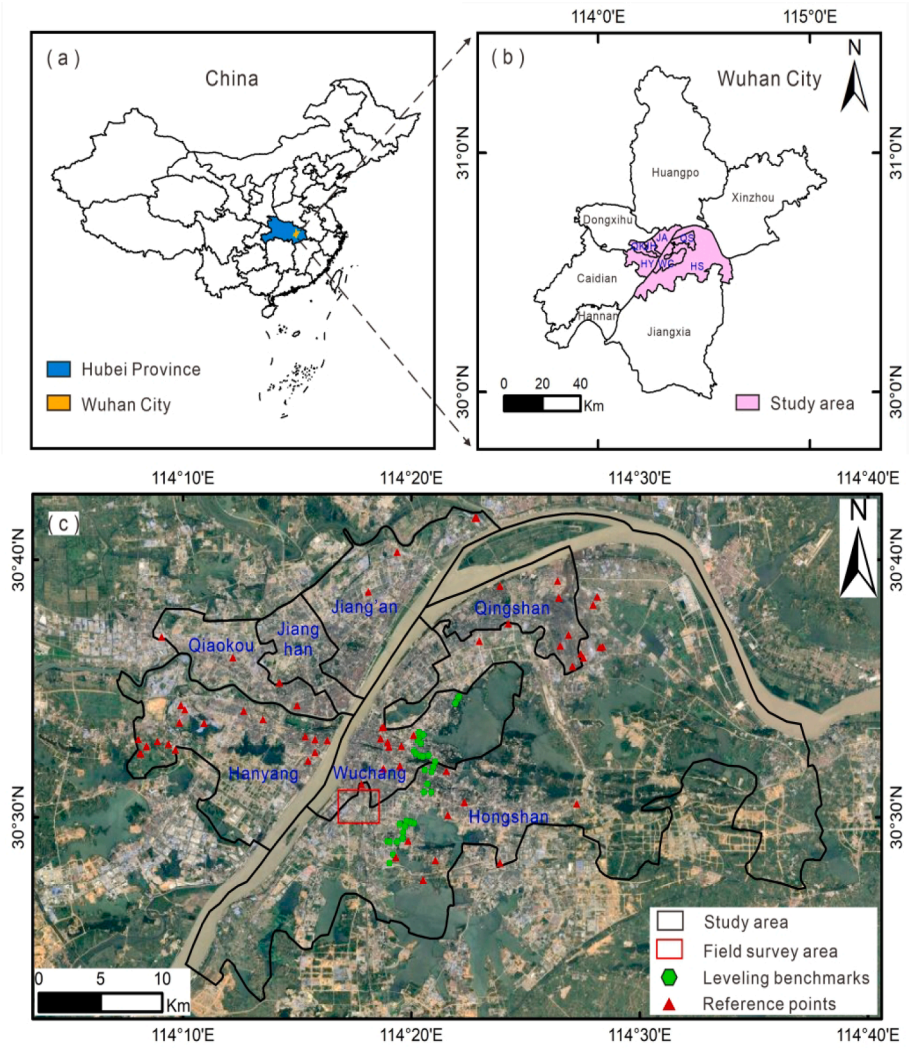

Fig. 1. The study area and the distribution of the field survey area, leveling benchmarks, and reference points.

Wuhan is high in the east and south, low in the west and north, with an average elevation of 23.3 m. Geomorphologically, Wuhan belongs to the hilly alluvial plain with widely distributed soft soils, leading to innate conditions for the occurrence of surface subsidence. Fig. 2 presents the consequences of subsidence during our field survey (highlighted by a red rectangle in Fig. 1) in Wuhan.

The subtropical monsoon climate brings sufficient rainfall, sunshine, and four distinct seasons to Wuhan. Its annual average temperature is the lowest in January and the highest in July. The total annual precipitation ranges from 1150 to 1450 mm, with most of the rainfall concentrating from June to August.

3. Data and methodology

3.1. Datasets

To obtain the high-frequency deformation results in Wuhan, we used 32 ascending C-band Sentinel-1A data published by the European Space Agency. The imaging time span was from January 2018 to August 2020, and the average time interval was about one month. These images were captured in VV (vertical-vertical) polarization and IW (interferometric wide) swath mode. Besides, the corresponding precise orbit ephemeris and elevation data were also obtained (Reuter et al., 2007) to correct the orbit information and remove the influence of systematic error and topographic phase on the deformation results.

Based on the SARscape platform, SBAS-InSAR (Berardino et al., 2002; Li et al., 2013) was selected to obtain time-series surface deformation results. The thresholds of temporal baseline and spatial baseline were 150 days and 180 m, respectively. As shown in Fig. 3, a total of 126 differential interferograms were generated. Uniformly distributed, highly coherent, stable reference points were selected to correct the interferometric phases by removing the constant and slope phases and provide support for the inversion of deformation results (Fig. 1(c)). The coherence threshold of the final pixels used for deformation rate estimation was 0.45. Besides, PS-InSAR (Deng et al., 2017; Ferretti et al., 2000) was selected to verify the reliability of the SBAS-InSAR results. The master image used in the PS-InSAR processing was obtained on July 7, 2019. Furthermore, the radar incident angle was used to transform the deformation into the vertical direction (Shi et al., 2021).

In addition, measurements from 33 high-precision leveling benchmarks (obtained from January 2018 to May 2018) were used to evaluate the accuracy of MT-InSAR results. These monitoring points were distributed in HS and WC (Fig. 1(c)). We also obtained the spatial distribution of waters, subway lines, soft soils, karst collapse prone areas, road density, population density, elevation, and annual average NDVI (Normalized Difference Vegetation Index) in the study area. The above natural and human factors were combined with the deformation results in the geo-detector to further analyze the spatial distribution and induced causes of subsidence.

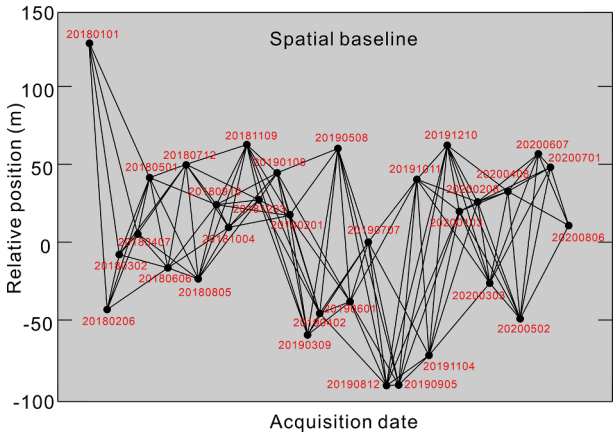

Fig. 3. The imaging time of Sentinel-1 data and the connection mode of interference image pairs.

3.2. Basic theory of geo-detector

Geo-detector is a statistical method used to detect spatial variability, aiming to reveal the driving factors behind phenomena (Wang et al., 2010; Wang and Xu, 2017). The core idea of the geo-detector is that if a factor has an important influence on an attribute, the spatial distribution of this factor and attribute should be similar. Three modules of geo-detector were used in this study: 1) differentiation and factor detection, 2) interaction detection, and 3) ecological detection.

The differentiation and factor detection module aims to detect the degree to which factor X explains the spatial differentiation of attribute Y. The range of q is [0,1], indicating that X explains $100 \times q\%$ of Y:

$$q = 1 - \frac{\sum_{h=1}^{L} N_h \sigma_h^2}{N\sigma^2} \tag{1}$$

where $h = 1, \cdots, L$ is the strata of factor X or attribute Y; N and σ^2 are the sample size and variance of attribute Y in the whole region, respectively;

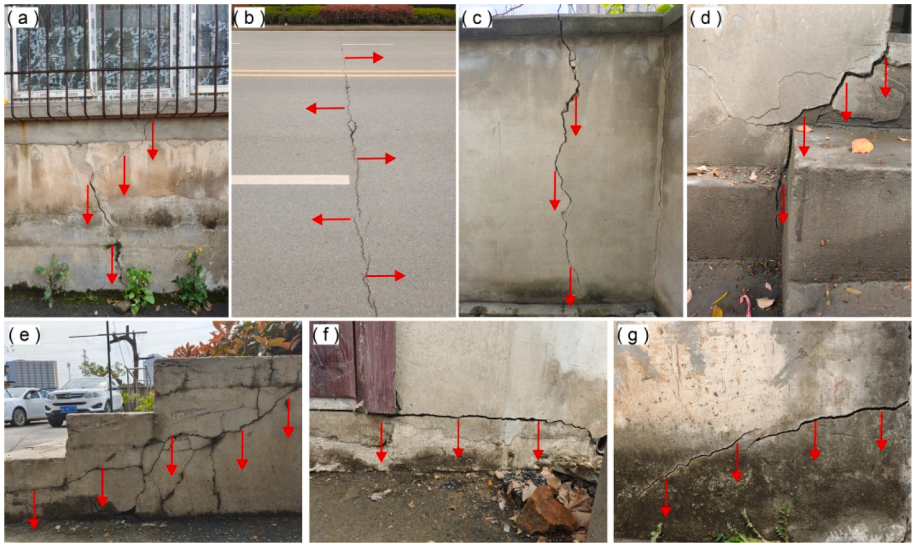

Fig. 2. Building wall cracks and road damage due to surface subsidence in the field survey area.

Table 1
The interaction detection result of two factors.

Criterion	Interaction
$q(X_1 \cap X_2) \langle Min(q(X_1), q(X_2)) \rangle$	Nonlinear weakening
$Min(q(X_1), q(X_2)) \langle q(X_1 \cap X_2) \langle Max(q(X_1), q(X_2)) \rangle$	Single factor nonlinear weakening
$q(X_1 \cap X_2)) Max(q(X_1), q(X_2)) \rangle$	Bilinear enhancement
$q(X_1 \cap X_2) = q(X_1) + q(X_2)$	Independent
$q(X_1 \cap X_2)) q(X_1) + q(X_2)$	Nonlinear enhancement

N_h and σ_h^2 are the sample size and variance of h layer attribute Y, respectively.

The interaction detection module aims to evaluate the explanatory power of the combined effect of factors X_1 and X_2 on attribute Y. Table 1 shows the possible interactions of two factors.

The ecological detection module aims to compare differences in explanatory importance of different factors, which is measured by F test:

$$F = \frac{N_{X_1}(N_{X_2} - 1)\sum_{h=1}^{L_1} N_h \sigma_h^2}{N_{X_2}(N_{X_1} - 1)\sum_{h=1}^{L_2} N_h \sigma_h^2} \tag{2}$$

where N_{X_1} and N_{X_2} represent the sample sizes of factors X_1 and X_2, respectively; L_1 and L_2 represent the layer number of factors X_1 and X_2, respectively.

3.3. The network structure of the LSTM model

LSTM can solve the problem of long-term dependency by reducing the occurrence of gradient disappearance (Hochreiter and Schmidhuber, 1997). The basic unit of LSTM consists of three gates, i.e., forgetting gate, input gate, and output gate (Fig. 4(b)), which discard unimportant information and retains important information by means of gate control, thus improving model learning ability.

Forgetting gate determines whether memory neurons need to clear the previous value:

$$f_t = \sigma(W_t[h_{t-1}, x_t] + b_f) \tag{3}$$

where σ is the *Sigmoid* function; W_t represents the weight matrix; h_{t-1} represents the output of the LSTM network at the upper layer; x_t represents the input; b_f represents the offset; f_t (ranging from 0 to 1) represents the degree of forgetting.

When the input gate is open, values are written into the memory neuron that selectively remembers the current input.

$$i_t = \sigma(W_i[h_{t-1}, x_t] + b_i) \tag{4}$$

$$\widetilde{C}_t = \mathrm{relu}(W_C[h_{t-1}, x_t] + b_C) \tag{5}$$

where i_t represents the input state and $\widetilde{C}_t$ represents the filter of i_t.

Forgetting gate and input gate together determine the state of the current network layer:

$$C_t = f_t * C_{t-1} + i_t * \widetilde{C}_t \tag{6}$$

The output gate controls whether the current state is output and what information can be used as output.

$$o_t = \sigma(W_o[h_{t-1}, x_t] + b_o) \tag{7}$$

$$h_t = o_t * \mathrm{relu}(C_t) \tag{8}$$

3.4. Experimental process

Complex geological background and rapid urbanization aggravate

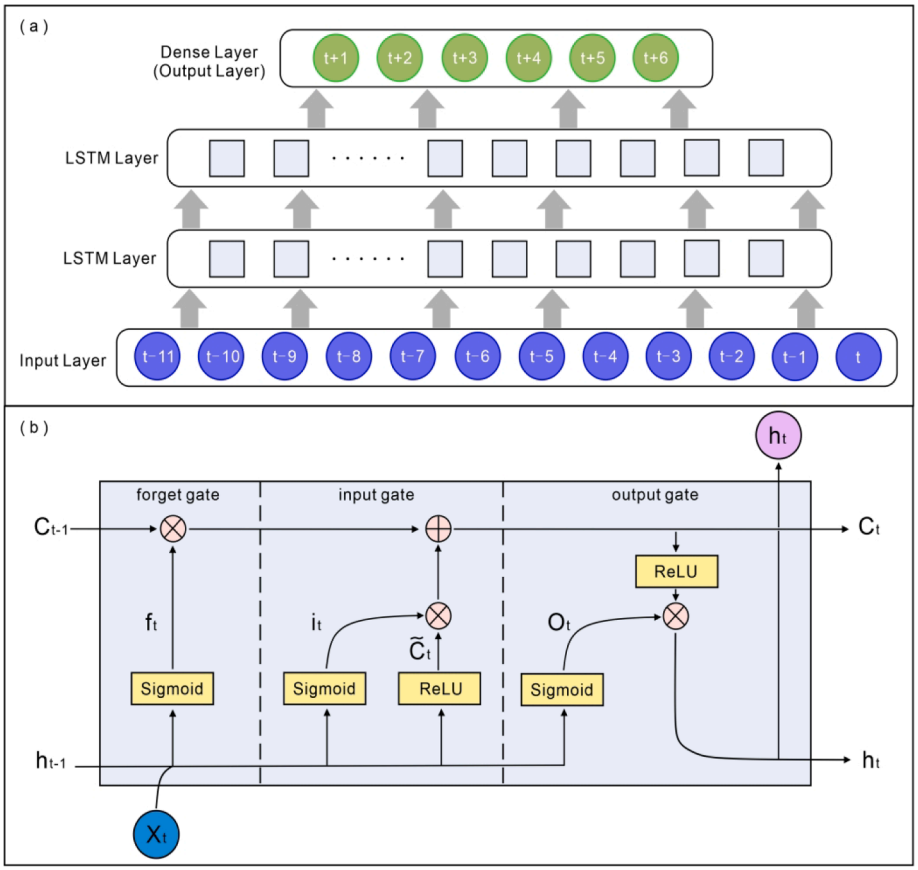

Fig. 4. (a) Network structure of LSTM model for predicting surface subsidence; (b) The basic computing unit of the LSTM model.

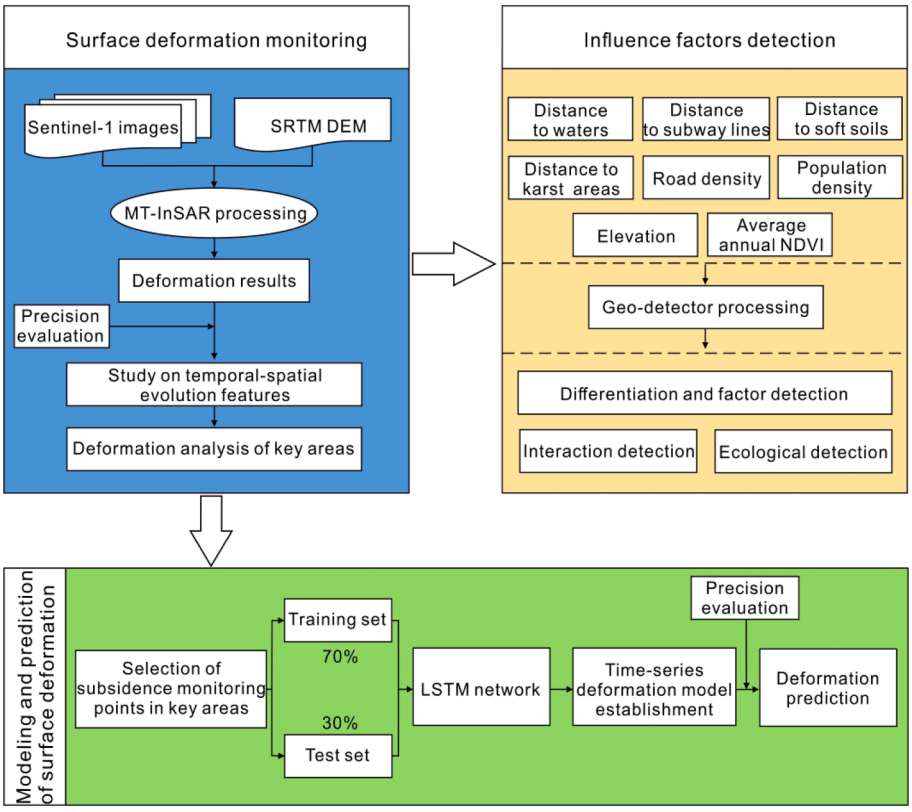

Fig. 5. The overall experimental workflow.

surface subsidence in Wuhan. In this study, MT-InSAR and Sentinel-1A data were used to obtain the surface deformation results. Based on the geo-detector model, the relationship between surface subsidence and a series of natural and human factors was analyzed. LSTM network was used to model and predict the time-series deformation in selected key subsidence regions. The overall process of the experiment is shown in Fig. 5.

4. Results

4.1. Spatiotemporal characteristics of surface deformation

A total of 714,711 deformation monitoring points were obtained, with an average density of 828/km^2. During the monitoring period, the maximum subsidence velocity and uplift velocity were −53.3 mm/year and 18.0 mm/year, respectively.

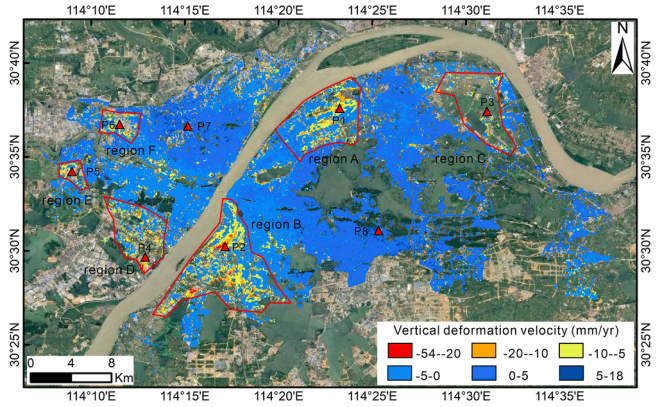

Fig. 6. Vertical surface deformation velocity in the study area.

From Fig. 6, we observed some newly emerged subsidence areas and further noticed that some old subsidence areas identified by existing studies tended to stabilize. For instance, the subsidence areas at JH and QK during 2009–2010 identified by Bai et al. (2016) and at JH and JA during 2015–2016 identified by Zhou et al. (2017) caused by urban construction have almost stabilized. Region A, located near the Nanganqu of QS, presented severer surface subsidence, which was similar to results extracted by Han et al. (2020), Shi et al. (2021), and Jiang et al. (2021). Region B, located near the Baishazhou of HS, was the newly formed subsidence area with greater severity than the results mentioned by Han et al. (2020) and Shi et al. (2021). We also acknowledged that the density of monitoring points in regions C and D was relatively low,

Table 2
Statistics of surface deformation in identified six regions.

Regions	A	B	C	D	E	F
Area (km^2)	35.0	56.7	27.9	23.5	4.5	7.8
Number of points	36,571	59,226	3024	9164	2703	6526
Maximum subsidence velocity (mm/year)	−31.7	−53.3	−29.3	−42	−20.3	−23.5
Maximum uplift velocity (mm/year)	7.6	6.7	5.2	3.7	3.4	3.9
Mean deformation velocity (mm/year)	−3.2	−5.0	−5.2	−4.8	−4.4	−3.4
Maximum cumulative subsidence (mm)	−76.1	−130.7	−78.9	−107.8	−56.8	−49.2
Maximum cumulative uplift (mm)	12.7	30.3	27.7	8.4	10.0	11.1
Mean cumulative deformation (mm)	−9.1	−12.1	−12.1	−15.6	−14.0	−8.0

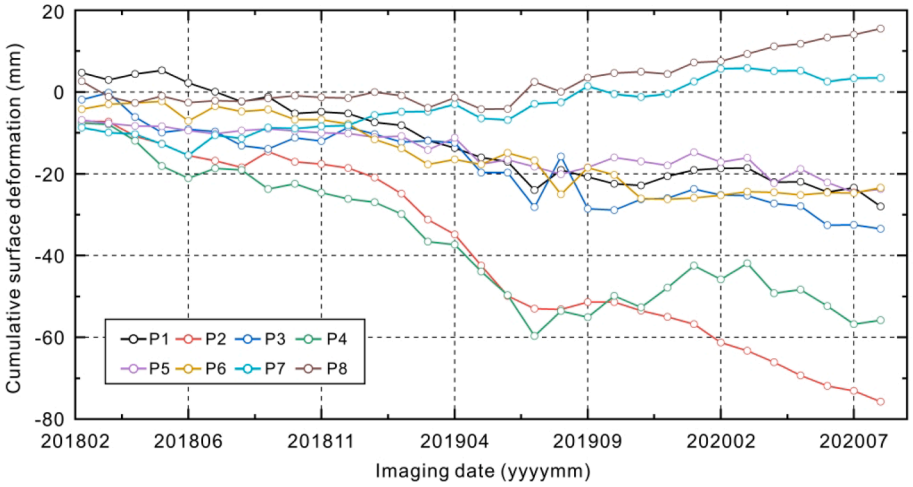

Fig. 7. Time-series cumulative surface deformation of eight typical monitoring points.

and regions E and F were relatively small in size. Statistics of surface deformation in identified six regions can be found in Table 2.

From Fig. 7, we observed that the time-series cumulative deformations at typical monitoring points (Fig. 6) present inconsistent trends. The cumulative subsidence at P2 located in region B was the largest, reaching −75.7 mm. Located in region D, P4 first experienced a subsidence process, then an uplift, followed by subsidence again. P1, P3, P5, and P6 were all in a slow subsidence state during the monitoring period. Although P7 presented an uplift pattern at the end, its cumulative deformation before September 2019 was negative. In comparison, P8 was relatively stable until June 2019 and has been on the rise since then. Note that, due to the short temporal span, monitoring points may be affected by accidental reasons, resulting in temporary deformation trends. Future works are needed to conduct long-term sequence analysis, aiming to obtain deformation trends with improved reliability.

4.2. Subsidence characteristics in key regions

As Regions A and B had abundant monitoring points and experienced severe subsidence, they were selected to further analyze the spatio-temporal characteristics of surface deformation.

From Fig. 8(a), (b), and (c), we observed that the subsidence center in region A shifted from southwest to northeast during the investigated period. By 2020, a large scale of surface subsidence appeared in the east of region A. The deformation velocity of 63.5% monitoring points was between −5 mm/year and 0 mm/year (Fig. 8(d)), indicating that region A was dominated by slow subsidence.

In addition, we noticed an area of excessive local land subsidence (highlighted by a black circle in Fig. 8(a)), located at the intersection of Enshi street and Gongye 1st road. The center of this area was closer to the M1 side (Fig. 8(e)). Along the line M1M2, the subsidence velocity varied from −7 mm/year to −14 mm/year.

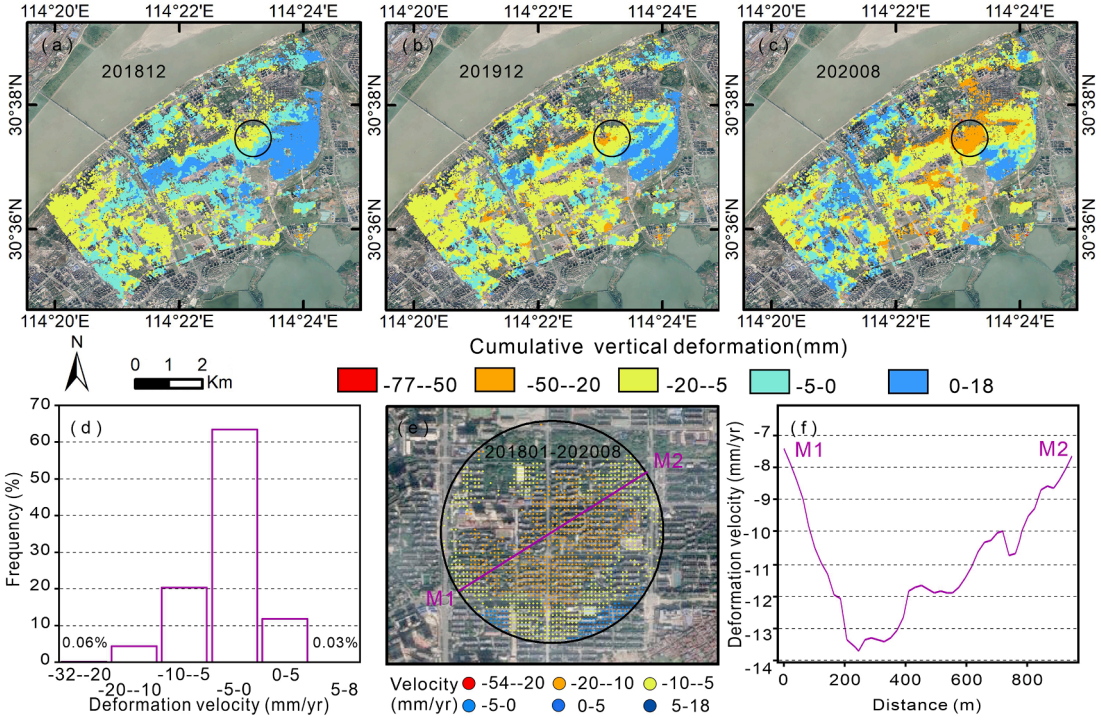

Fig. 8. Cumulative surface deformation in region A from January 2018 to (a) December 2018; (b) December 2019; (c) August 2020; (d) Frequency distribution of deformation velocity; (e) Velocity in the localized subsidence and the position of line M1M2; (f) Variation of deformation velocity along line M1M2.

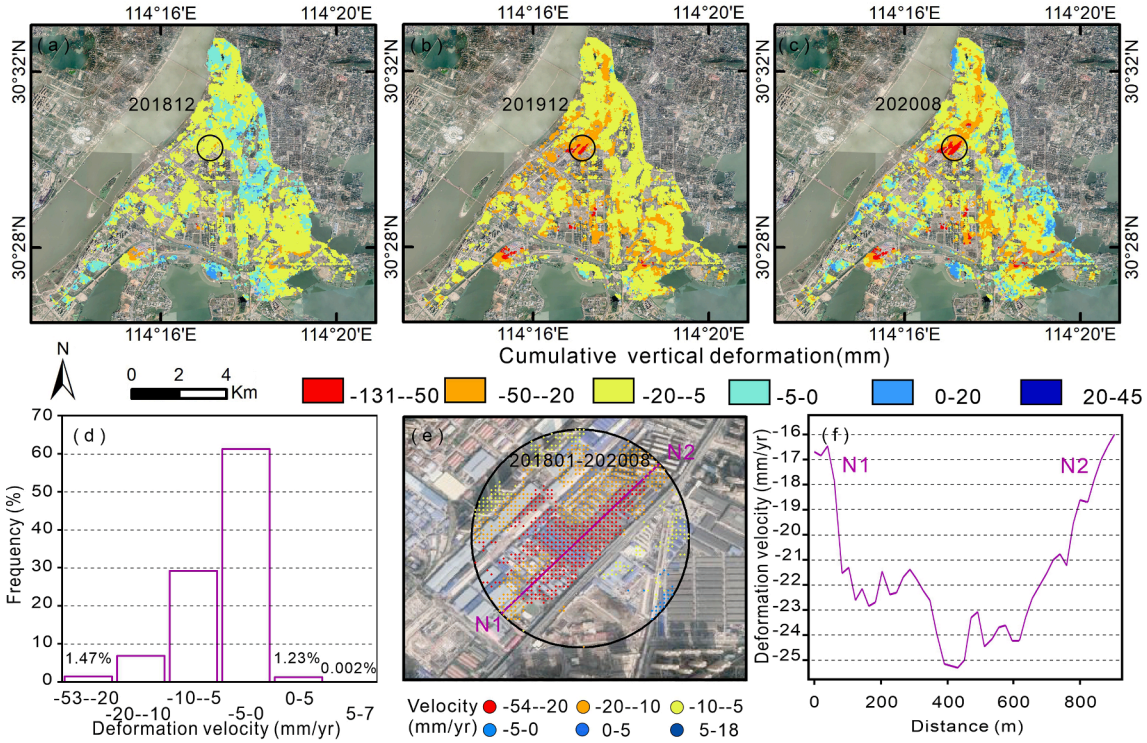

Fig. 9. Cumulative surface deformation in region B from January 2018 to (a) December 2018; (b) December 2019; (c) August 2020; (d) Frequency distribution of deformation velocity; (e) Velocity in the localized subsidence and the position of line N1N2; (f) Variation of deformation velocity along line N1N2.

In 2018 and 2019, region B showed a state of subsidence. In 2020, however, part of region B uplifted. During the monitoring period, the deformation velocity of the 61.25% monitoring points ranged from −5 mm/year to 0 mm/year (Fig. 9(d)). Similar to region A, we also identified localized subsidence in region B, which was located near Baishazhou avenue. Combined with Fig. 9(a), (b), (c), and the P2 time-series deformation in Fig. 7, we can conclude that this area was in continuous annual subsidence during the investigated period. Along line N1N2 in this area, the maximum surface subsidence rate exceeded −25 mm/year.

4.3. Accuracy assessment of MT-InSAR results

Based on PS-InSAR, 32 Sentinel-1 images were processed again. The internal accuracy was evaluated by comparing the differences between PS-InSAR and SBAS-InSAR results (Fig. 10).

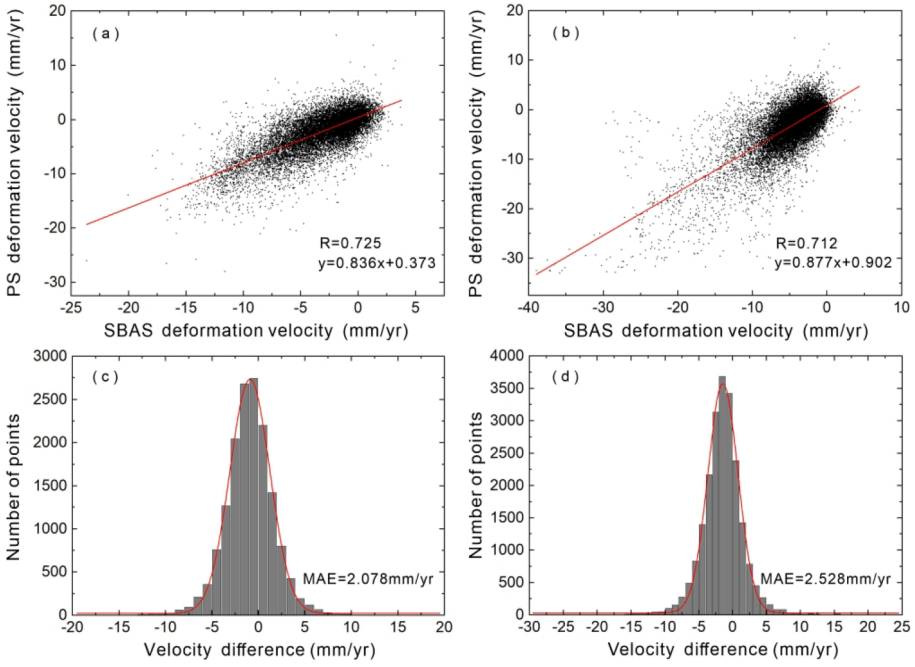

Fig. 10. Scatterplot of deformation velocity between PS-InSAR and SBAS-InSAR in (a) region A; (b) region B; Distribution of velocity difference in (c) region A; (d) region B.

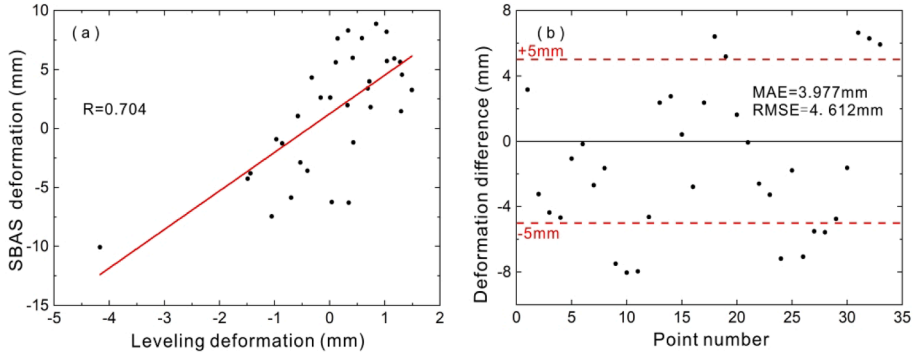

Fig. 11. (a) Scatterplot of deformation between SBAS-InSAR and leveling; (b) Differences in deformation measurement from SBAS-InSAR and leveling.

In region A, there were a total of 15,557 corresponding points between PS-InSAR and SBAS-InSAR results. The deformation velocities from different MT-InSAR results showed a strong positive correlation (R = 0.725). The velocity difference of 93.37% corresponding points was within ±5 mm/year. The MAE (mean absolute error) of the velocity difference was 2.078 mm/year. In region B, the correlation coefficient R was 0.712, and the MAE was 2.528 mm/year. The above results largely confirmed the reliability of MT-InSAR in monitoring surface subsidence.

In addition, the nearest SBAS-InSAR monitoring point (less than 20 m) towards a certain benchmark was selected to compare with that benchmark (Fig. 11). SBAS-InSAR results were positively correlated with leveling results (R = 0.704). The MAE and RMSE (root mean squared error) of deformation difference were 3.977 mm and 4.612 mm, respectively, proving that MT-InSAR is able to measure deformation in an accurate manner.

5. Discussion

5.1. Relationship between surface subsidence and influencing factors

Geo-detector was used to analyze the relationship between the spatial characteristics of subsidence and the influencing factors. The natural factors include elevation, NDVI, distribution of waters, soft soils, and karst collapse prone areas. Human factors include subway lines, population and road density.

Fig. 12 shows the surface deformation results and the related influencing factors. The qualitative analysis indicated that the subsidence areas in Wuhan (Fig. 12(a)) were mostly distributed in areas covered by soft soils (Fig. 12(f)), and the subsidence areas had relatively low elevation (Fig. 12(h)). In addition, no obvious correlation was found between the spatial distribution of subsidence and other factors.

In order to further quantitatively analyze the exact influence of various factors on the subsidence distribution, 5000 random points were selected in MT-InSAR results (Fig. 12(a)). The deformation velocity at random points was extracted as attribute Y, while the distance to waters (X_1), distance to subway lines (X_2), distance to soft soils (X_3), distance to karst collapse prone areas (X_4), elevation (X_5), population density (X_6), road density (X_7), and annual average NDVI (X_8) were extracted as factors X. Jenks Natural Breaks method was used to divide each factor into six categories. Then, we imported independent variable X and attribute Y into the geo-detector for differentiation and factor detection, interaction detection, and ecological detection.

Table 3 reveals that p values for all the factors were 0, indicating that all factors had a significant impact on the spatial differentiation of subsidence. The distance to soft soils (X_3) was the most important factor affecting the spatial distribution of subsidence with a q value of 0.184. The elevation (X_5) was the second with a q value of 0.106. This finding was consistent with qualitative analysis, which again proved that the distribution of soft soils and elevation were the two main factors to explain the spatial distribution of surface subsidence.

In addition, the q values of annual average NDVI (X_8) and distance to karst collapse prone areas (X_4) were 0.064 and 0.051, respectively, suggesting that the NDVI and the karst collapse also had a certain correlation with subsidence distribution. Among them, annual NDVI can represent the difference in vegetation coverage, reflecting the land covers to a certain extent. Soil parameters (e.g., water content, void ratio, and strength) of areas with different annual NDVI are diverse, which may have an impact on the distribution of surface subsidence. The q values of distance to waters (X_1), distance to subway lines (X_2), population density (X_6), and road density (X_7) were less than 0.05, indicating that these factors had a considerably trivial influence on the subsidence distribution.

Based on geo-detector, the results of interaction detection and ecological detection were obtained (Fig. 13). The results suggested that the spatial distribution of subsidence in Wuhan was jointly affected by multiple factors. Compared with a single factor, the interaction of two factors had a greater influence on the subsidence. According to the criterion shown in Table 1, except for the bilinear enhancement between X_3 and X_8, and between X_3 and X_5, the interaction patterns between two factors were nonlinear enhancement.

The interaction between the distance to soft soils and the distance to karst collapse prone areas had the largest explanatory power on the surface subsidence with a q value of 0.303. This result indicated that the spatial distribution and differentiation of surface subsidence in Wuhan were mainly affected by nature-induced factors. What's more, 18 pairs of factors from ecological detection had no significant difference in explaining the spatial characteristics of subsidence when either two factors were combined.

5.2. Modeling and predicting time-series surface subsidence

Studies have shown that the surface subsidence in Wuhan affected by evaluative factors is place-dependent (Bai et al., 2016; Han et al., 2020; Jiang et al., 2021; Shi et al., 2021; Zhou et al., 2017). Therefore, building different models given different regions is expected to achieve more accurate subsidence prediction. In this study, the key regions A and B were taken as the experimental areas, and the LSTM model was proposed to predict the time series of cumulative deformation. We defined "rapid subsidence" as monitoring points moving faster than −5 mm/year. Datasets were created by collecting time-series cumulative deformation of rapid subsidence points in both regions A and B. In order to verify the accuracy of the model, these two datasets (Fig. 14) were both randomly divided into a training set (70%) and a test set (30%).

The cumulative vertical deformation of 12 consecutive periods was taken as the input to ensure that the model learns reliable contextual features. Since the model accuracy deteriorates with the increase of the output periods, the cumulative vertical deformation of the following six periods (half of the input) was taken as the output to ensure the reliability of the prediction results. For any time t, the input of the model was the cumulative vertical deformation $[D_{t-11}, D_{t-10}, \cdots, D_t]$ and the

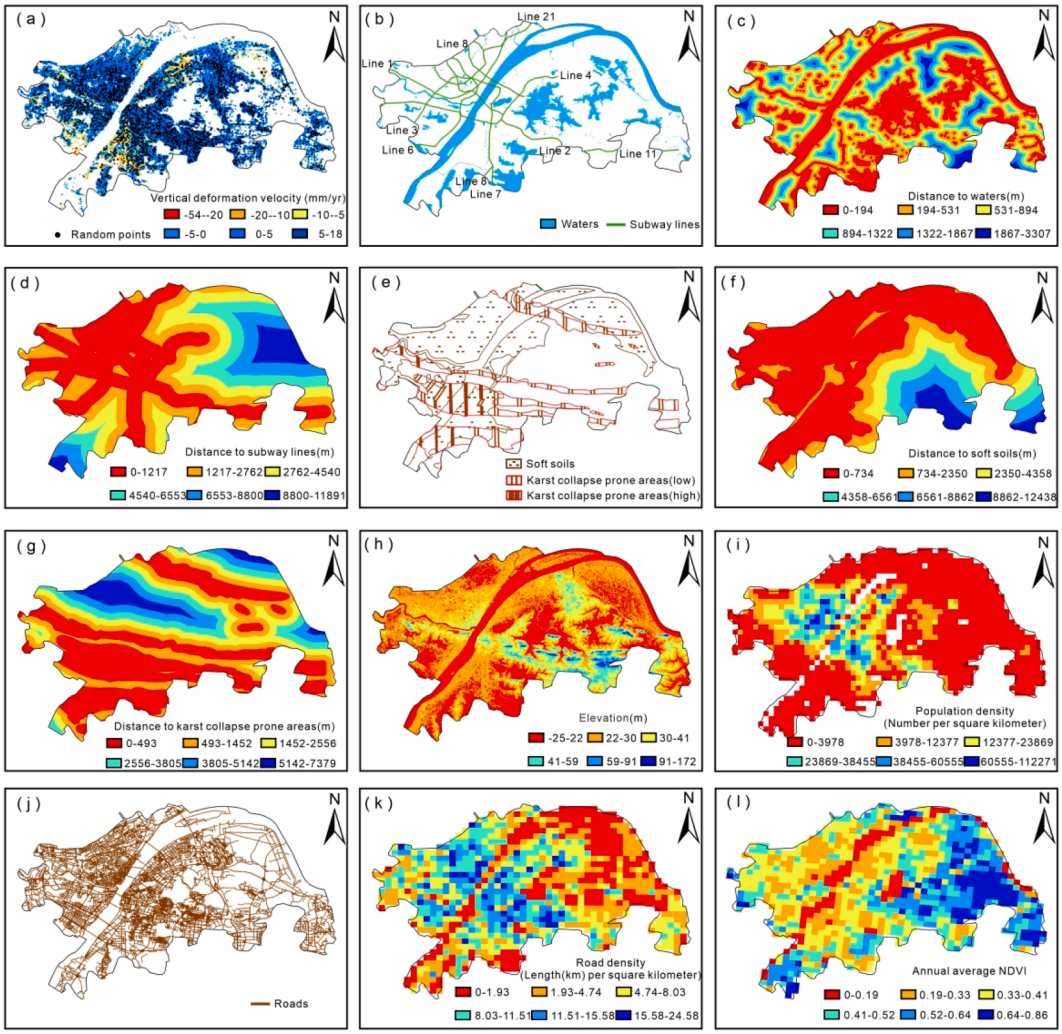

Fig. 12. (a) Deformation velocity the distribution of random points; (b) Distribution of waters and subway lines; (c) Distance to waters; (d) Distance to subway lines; (e) Distribution of soft soils and karst collapse prone areas; (f) Distance to soft soils; (g) Distance to karst collapse prone areas; (h) Elevation; (i) Population density; (j) Distribution of roads; (k) Road density; (l) Annual average NDVI.

Table 3
The results of differentiation and factor detection.

Factor	X_1	X_2	X_3	X_4	X_5	X_6	X_7	X_8
q statistic	0.008	0.027	0.184	0.051	0.106	0.009	0.027	0.064
p value	0.000	0.000	0.000	0.000	0.000	0.000	0.000	0.000

output was $[D_{t+1}, D_{t+2}, \cdots, D_{t+6}]$.

All time-series records were fed into the LSTM model (Fig. 4(a)) in a rolling manner. The number of neurons in each LSTM layer was set to 50. The learning rate was set to 0.001, MSE (mean squared error) was selected as the loss function, the optimizer was Adam optimizer, and the epochs were set to 60. After the training, the results of the test points in regions A and B are shown in Tables 4 and 5, respectively.

We observed that the accuracy of the LSTM model was the highest in time $t+1$ and gradually decreased with the increase of time span. Nevertheless, it still achieved great predicting performance at the time $t+6$, with MAE less than 2.6 mm and R^2 more than 0.8, proving that the proposed LSTM was effective in predicting time-series subsidence.

Eight test points were selected (Fig. 14) to further evaluate the performance of the LSTM model. There existed a temporal overlap between the MT-InSAR monitoring results and LSTM predicted results from October 2019 to August 2020, i.e., from D_{13} to D_{32}. Within the overlapping time span, when any time was taken as time $t+1$, the predicted results were taken as its final results. Outside the overlapping time span, i.e., from September 2020 to February 2021 (D_{33} to D_{38}), the cumulative deformation from September 2019 to August 2020 (D_{21} to D_{32}) was used as input to obtain the final prediction.

We observed that different test points presented varying subsidence processes (Fig. 15). For example, point A2 presented approximately linear subsidence; point A4 had a "stable-subsidence-stable" process; points B3 and B4 presented a "V" shape pattern, as they experienced significant subsidence but followed by uplifts. Predictions from LSTM and the results from MT-InSAR showed high consistency with limited errors, demonstrating that our LSTM model can efficiently mine the features of time-series deformation with different patterns in a self-adaptive manner.

After verifying the accuracy and reliability of the proposed LSTM model, it was applied to predict and analyze the deformation of the rapid

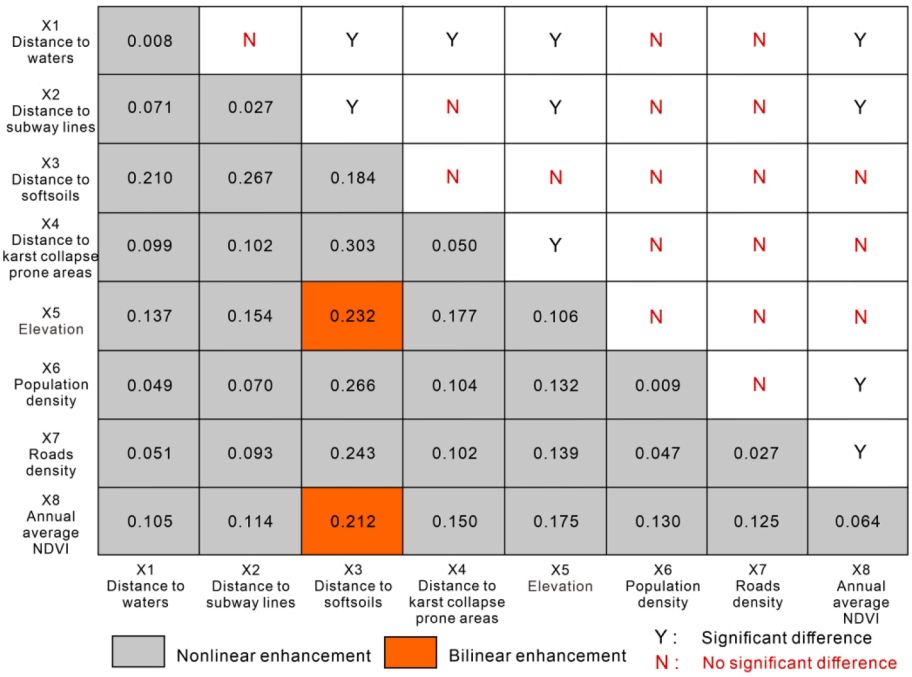

Fig. 13. The results of interaction detection and ecological detection.

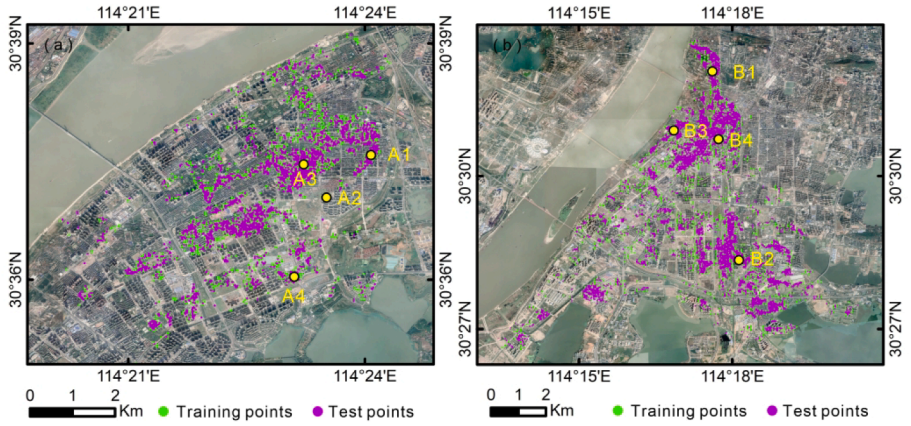

Fig. 14. The spatial distribution of training points and test points in (a) region A; (b) region B. Note that occlusion occurs between the training and test points, given the high density of the rapid subsidence points.

Table 4
Accuracy evaluation of LSTM prediction results in region A.

Time	$t+1$	$t+2$	$t+3$	$t+4$	$t+5$	$t+6$
MAE	1.3775	1.4648	1.6480	1.7691	1.9183	2.1242
R^2	0.9243	0.9083	0.8795	0.8563	0.8291	0.8080
MSE	3.5627	4.1550	5.2311	6.2350	7.4567	9.0657
RMSE	1.8875	2.0384	2.2872	2.4970	2.7307	3.0109

Table 5
Accuracy evaluation of LSTM prediction results in region B.

Time	$t+1$	$t+2$	$t+3$	$t+4$	$t+5$	$t+6$
MAE	1.4772	1.6116	1.8450	2.0393	2.2968	2.5273
R^2	0.9579	0.9482	0.9333	0.9197	0.9021	0.8896
MSE	4.0058	4.8162	6.2814	7.9695	10.0670	12.1556
RMSE	2.0014	2.1946	2.5063	2.8230	3.1729	3.4865

subsidence points in regions A (Fig. 16) and B (Fig. 17).

According to the prediction results, the localized subsidence in region A (see the black circle in Fig. 16(a)) had decreased from September 2020 to February 2021. The southwest part of region A (see the black rectangle in Fig. 16(a)) was in the process of continuous subsidence. In comparison, the localized subsidence in region B, although presenting intensified surface subsidence in the central part, had not changed greatly in terms of the position and size.

6. Conclusions

In this study, we used MT-InSAR and Sentinel-1 data to investigate the surface deformation in Wuhan. Furthermore, the relationship between surface subsidence and nature- and human-induced factors were quantitatively analyzed, and the time-series surface subsidence was predicted. The main conclusions are as follows:

(1) The surface subsidence in Wuhan was obvious and unevenly distributed. From January 2018 to August 2020, deformation

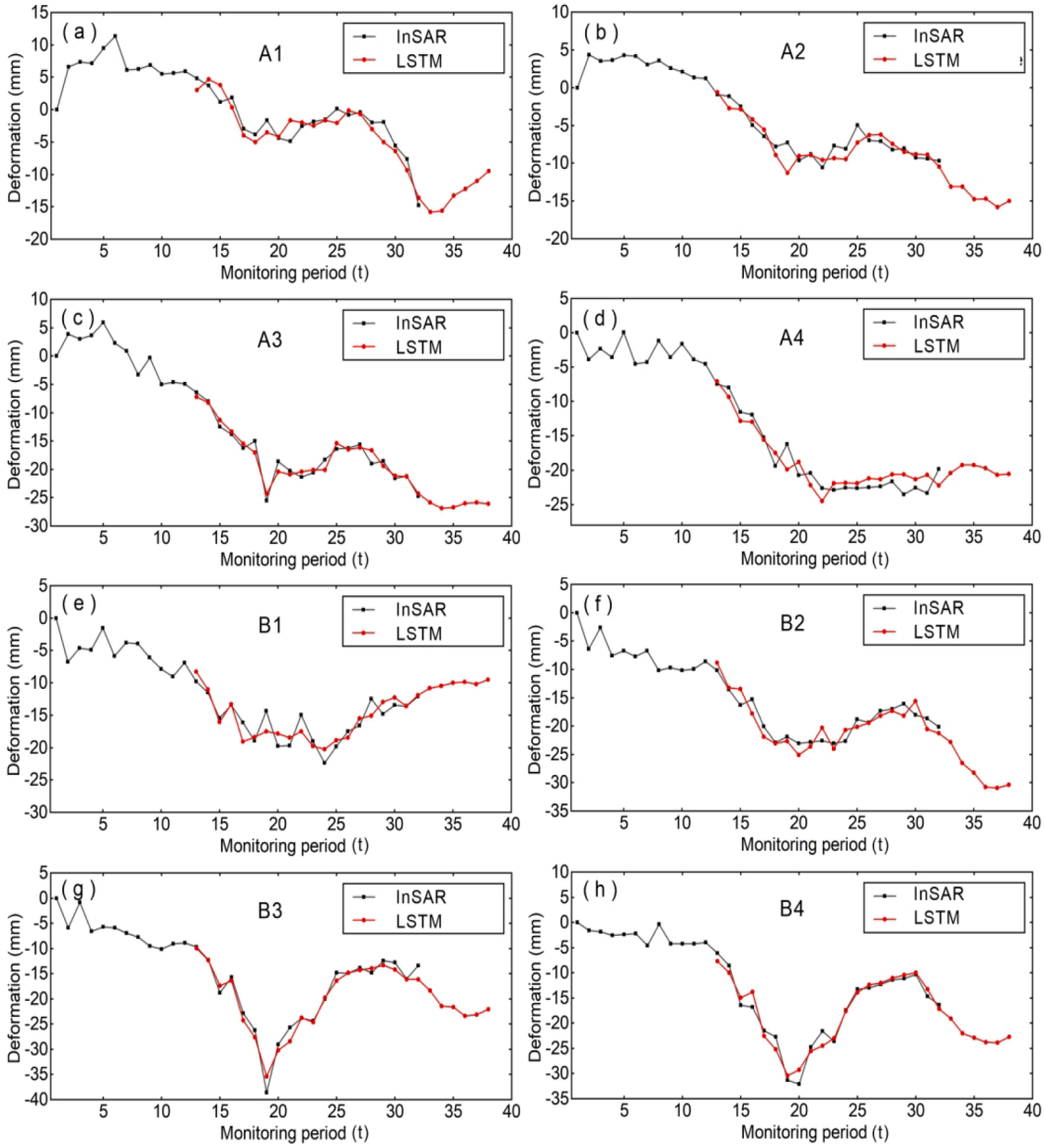

Fig. 15. Time-series cumulative deformation predicted by LSTM model and monitored by MT-InSAR.

velocity ranged from −53.3 mm/year to 18.0 mm/year. The severest surface subsidence occurred in Baishazhou of HS, with the maximum cumulative subsidence reaching −130.7 mm. The comparison of SBAS-InSAR results with PS-InSAR results and leveling observations verified the reliability of MT-InSAR in surface deformation monitoring.

(2) The distance to soft soils (q value of 0.184) was the most important factor that affects the spatial distribution of subsidence. However, the spatial distribution of subsidence was determined via the coupling effects from multiple factors (no independent influence was found). The distance to soft soils and the distance to karst collapse prone areas had the largest joint influence (q value of 0.303) on the spatial distribution of surface subsidence.

(3) The proposed data-driven LSTM model achieved great performance, despite that its prediction accuracy decreased slightly with the increase of time span. The predicted results from LSTM were highly consistent with measurement from MT-InSAR, with MAE less than 2.6 mm and R^2 greater than 0.8 at the time $t + 6$. In addition, the proposed LSTM model was able to achieve consistently high performance over locations that presented different patterns of surface subsidence.

(4) Future works are needed to conduct longer-term and higher-resolution time-series surface deformation monitoring and analysis. With longer-period monitoring, we plan to introduce the spatial neighborhood relationship of high-density monitoring points into the model so as to achieve more accurate predicted results of long-period surface subsidence.

CRediT authorship contribution statement

Qing Ding: Methodology, Software, Writing - original draft. **Zhenfeng Shao:** Data curation, Visualization, Investigation. **Xiao Huang:** Writing - review & editing. **Orhan Altan:** Software, Validation. **Qingwei Zhuang:** Conceptualization, Validation. **Bin Hu:** Methodology.

Declaration of Competing Interest

The authors declare that they have no known competing financial interests or personal relationships that could have appeared to influence the work reported in this paper.

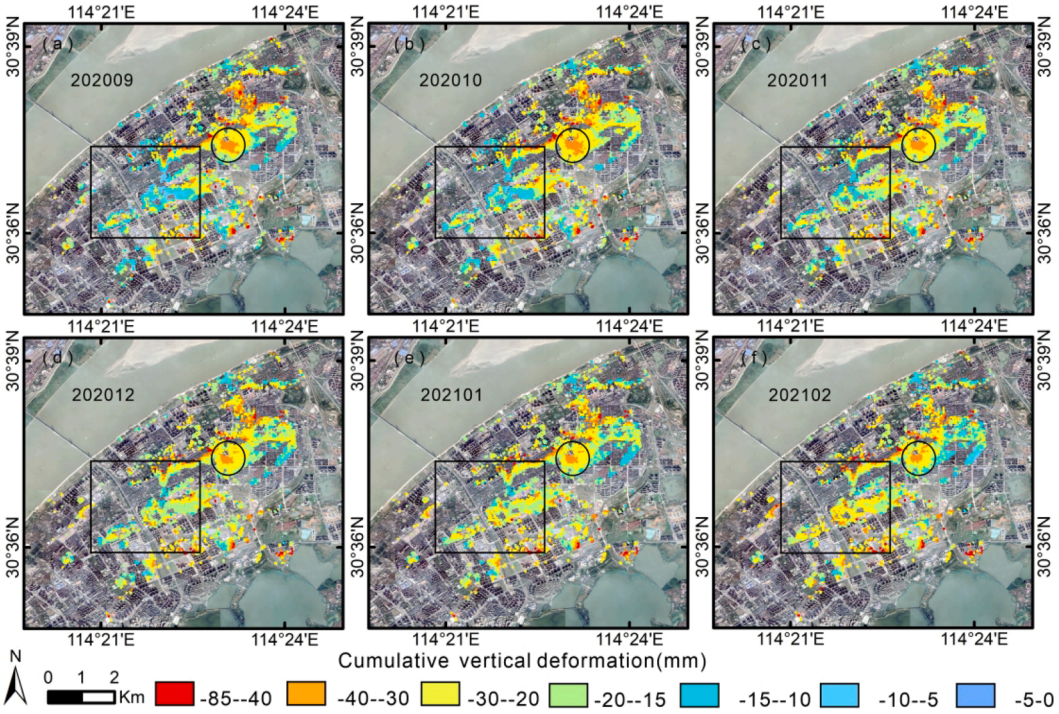

Fig. 16. Predictions of cumulative deformation in region A from January 2018 to (a) September 2020; (b) October 2020; (c) November 2020; (d) December 2020; (e) January 2021; (f) February 2021.

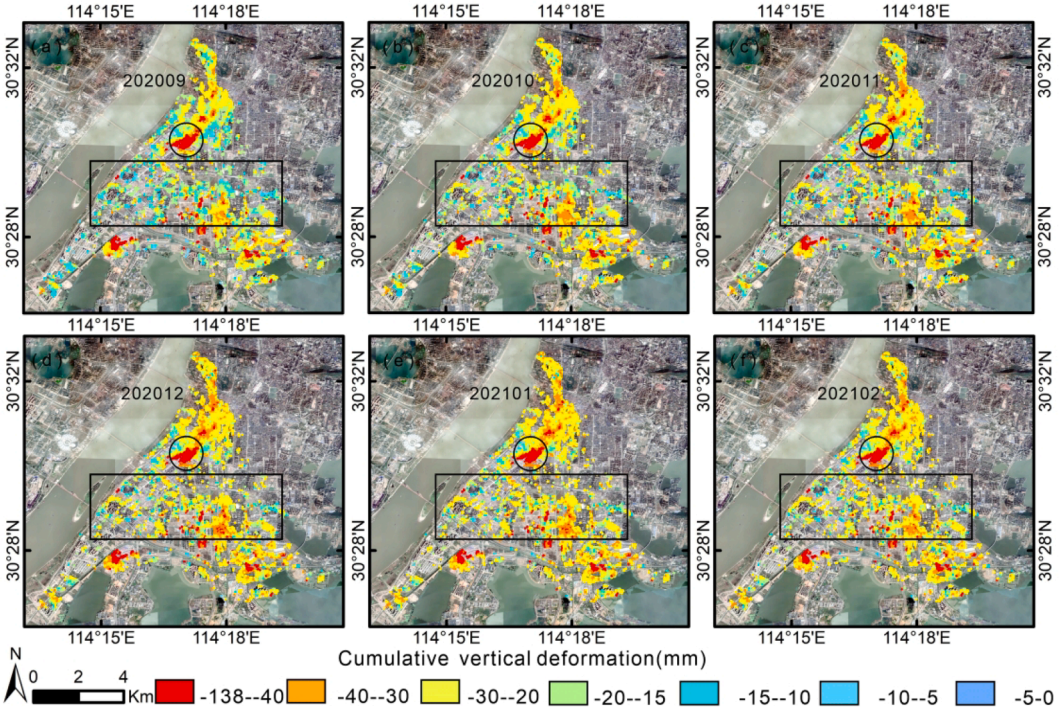

Fig. 17. Predictions of cumulative deformation in region B from January 2018 to (a) September 2020; (b) October 2020; (c) November 2020; (d) December 2020; (e) January 2021; (f) February 2021.

Acknowledgements

This work was supported in part by the National Key R&D Program of China under Grant 2018YFB2100501; in part by the National Natural Science Foundation of China under Grants 42090012, 41771452, 41771454; in part by the Key R&D Program of Yunnan Province in China under Grant 2018IB023.

References

Amelung, F., Galloway, D.L., Bell, J.W., Zebker, H.A., Laczniak, R.J., 1999. Sensing the ups and downs of Las Vegas: InSAR reveals structural control of land subsidence and aquifer-system deformation. Geology 27 (6), 483–486.

Babaee, S., Mousavi, Z., Masoumi, Z., Aflaki, M., Malekshah, A.H., Roostaei, M., 2020. Land subsidence from interferometric SAR and groundwater patterns in the Qazvin plain. Iran. Int. J. Remote Sens. 41 (12), 4778–4796.

Bai, L., Jiang, L., Wang, H., Sun, Q., 2016. Spatiotemporal Characterization of Land Subsidence and Uplift (2009–2010) over Wuhan in Central China Revealed by TerraSAR-X InSAR Analysis. Remote Sens., 8(4), 350–350.

Berardino, P., Fornaro, G., Lanari, R., Sansosti, E., 2002. A new algorithm for surface deformation monitoring based on small baseline differential SAR interferograms. IEEE Trans. Geosci. Remote Sens. 40 (11), 2375–2383.

Cigna, F., Osmanoğlu, B., Cabral-Cano, E., Dixon, T.H., Ávila-Olivera, J.A., Garduño-Monroy, V.H., DeMets, C., Wdowinski, S., 2012. Monitoring land subsidence and its induced geological hazard with Synthetic Aperture Radar Interferometry: a case study in Morelia. Mexico. Remote Sens. Environ. 117, 146–161.

Deng, Z., Ke, Y., Gong, H., Li, X., Li, Z., 2017. Land subsidence prediction in Beijing based on PS-InSAR technique and improved Grey-Markov model. GIsci. Remote Sens. 54 (6), 797–818.

Du, Z., Ge, L., Ng, A.H.-M., Zhu, Q., Yang, X., Li, L., 2018. Correlating the subsidence pattern and land use in Bandung, Indonesia with both Sentinel-1/2 and ALOS-2 satellite images. Int. J. Appl. Earth Obs. 67, 54–68.

Ferretti, A., Prati, C., Rocca, F., 2000. Nonlinear subsidence rate estimation using permanent scatterers in differential SAR interferometry. IEEE Trans. Geosci. Remote Sens. 38 (5), 2202–2212.

Jiang, H., Balz, T., Cigna, F., Tapete, D., 2021. Land subsidence in Wuhan revealed using a non-linear PSInSAR approach with long time series of COSMO-SkyMed SAR data. Remote Sens. 13, 1256.

Han, Y., Zou, J., Lu, Z., Qu, F., Kang, Y., Li, J., 2020. Ground deformation of wuhan, china, revealed by multi-temporal InSAR analysis. Remote Sens. 12 (22), 3788.

Hochreiter, S., Schmidhuber, J., 1997. Long short-term memory. Neural Comput. 9 (8), 1735–1780.

Kim, S.-W., Wdowinski, S., Dixon, T. h., Amelung, F., Kim, J. W., Won, J.-S., 2010. Measurements and predictions of subsidence induced by soil consolidation using persistent scatterer InSAR and a hyperbolic model. Geophys. Res. Lett., 37(5).

Li, S., Li, Z., Hu, J., Sun, Q., Yu, X., 2013. Investigation of the Seasonal oscillation of the permafrost over Qinghai-Tibet Plateau with SBAS-InSAR algorithm. Acta Geophys. Sin. 56 (5), 1476–1486.

Lu, Y., Ke, C., Jiang, H., Chen, D., 2019. Monitoring urban land surface deformation (2004–2010) from InSAR, groundwater and levelling data: a case study of Changzhou city. China. J. Earth Syst. Sci. 128 (6).

Lorenzo, A., Nicola, M., Ricardo, A., Chester, S., Diego, D., 2020. Monitoring Land Surface Deformation Associated with Gold Artisanal Mining in the Zaruma City (Ecuador). Remote Sens., 12, 2135–2135.

Luo, C., Li, X., Ye, Y., 2021. PFST-LSTM: a SpatioTemporal LSTM model with pseudoflow prediction for precipitation nowcasting. IEEE J. Sel. Top. Appl. Earth Obs. Remote Sens. 14, 843–857.

Mu, L., Wang, L., Wang, Y., Chen, X., Han, W., 2019. Urban land use and land cover change prediction via self-adaptive cellular based deep learning with multisourced data. IEEE J. Sel. Top. Appl. Earth Obs. Remote Sens. 12 (12), 5233–5247.

Osmanoğlu, B., Dixon, T.H., Wdowinski, S., Cabral-Cano, E., Jiang, Y., 2011. Mexico City subsidence observed with persistent scatterer InSAR. Int. J. Appl. Earth Obs. 13 (1), 1–12.

Perissin, D., Wang, Z., Lin, H., 2012. Shanghai subway tunnels and highways monitoring through Cosmo-SkyMed Persistent Scatterers. ISPRS J. Photogramm. Remote Sens. 73, 58–67.

Qu, F., Lu, Z., Zhang, Q., Bawden, G.W., Kim, J.-W., Zhao, C., Qu, W., 2015. Mapping ground deformation over Houston-Galveston, Texas using multi-temporal InSAR. Remote Sens. Environ. 169, 290–306.

Reuter, H.I., Nelson, A., Jarvis, A., 2007. An evaluation of void-filling interpolation methods for SRTM data. Int. J. Geogr. Inf. Sci. 21 (9), 983–1008.

Shi, X., Zhang, S., Jiang, M., Pei, Y., Qu, T., Xu, J., Yang, C., 2021. Spatial and temporal subsidence characteristics in Wuhan city (China) during 2015–2019 inferred from Sentinel-1 SAR Interferometry. Nat. Hazard. Earth Sys. 1–20.

Wang, F., Ding, Q., Wang, M., Zhang, L., Wang, Q., 2019. Analysis of land surface deformation in Chagan Lake region using TCPInSAR. Sustainability 11 (18).

Wang, J., Li, X., Christakos, G., Liao, Y., Zhang, T., Gu, X., Zheng, X., 2010. Geographical detectors-based health risk assessment and its application in the neural tube defects study of the heshun region. China. Int. J. Geogr. Inf. Sci. 24 (1), 107–127.

Wang, J., Xu, C., 2017. Geodetector: Principle and prospective. Acta Geophys. Sin. 72 (1), 116–134.

Xu, X., Tong, T., Zhang, W., Meng, L., 2020. Fine-grained prediction of PM2.5 concentration based on multisource data and deep learning. Atmos. Pollut. Res. 11 (10), 1728–1737.

Zhang, L., Ding, X., Lu, Z., 2011. Modeling PSInSAR time series without phase unwrapping. IEEE Trans. Geosci. Remote Sens. 49 (1), 547–556.

Zhang, L., Ding, X., Lu, Z., Jung, H.S., Hu, J., Feng, G., 2014. A novel multitemporal InSAR model for joint estimation of deformation rates and orbital errors. IEEE Trans. Geosci. Remote Sens. 52 (6), 3529–3540.

Zhou, L., Guo, J., Hu, J., Li, J., Xu, Y., Pan, Y., Shi, M., 2017. Wuhan surface subsidence analysis in 2015–2016 based on Sentinel-1A data by SBAS-InSAR. Remote Sens. 9 (10), 982.

Zhou, W., Chen, F., Guo, H., 2015. Differential radar interferometry for structural and ground deformation monitoring: a new tool for the conservation and sustainability of cultural heritage sites. Sustainability 7 (2), 1712–1729.